Plasma-catalytic synthesis of ammonia over $Ru/BaTiO_3$-based bimetallic catalysts: Synergistic effect from dual-metal active sites

Jin Liu[a], Xinbo Zhu[a,*], Susu Jiang[a], Hao Zhang[b], Yu Hong[a,c,d], Geng Chen[a], Xin Tu[e,**]

a. Faculty of Maritime and Transportation, Ningbo University, Ningbo, 315211, P.R. China

b. State Key Laboratory of Clean Energy Utilization, Institute for Thermal Power Engineering, Zhejiang University, Hangzhou, 310027, P.R. China

c. New Materials Institute, University of Nottingham Ningbo China, Ningbo, 315100, P.R. China

d. Research and Development Center, Ningbo Energy Group Co. Ltd, Ningbo, 315040, P.R. China

e. Department of Electrical Engineering and Electronics, University of Liverpool, Liverpool, L69 3GJ, UK

Abstract

Plasma-catalytic synthesis of ammonia (NH_3) was carried out using $BaTiO_3$ supported Ru-M bimetallic catalysts ($Ru-M/BaTiO_3$, M = Fe, Co and Ni) in a dielectric barrier discharge (DBD) reactor. The NH_3 synthesis performance followed the order of $Ru-Ni/BaTiO_3$ > $Ru/BaTiO_3$ > $Ru-Co/BaTiO_3$ > $Ru-Fe/BaTiO_3$, with the highest NH_3 concentration (3895 ppm) and energy yield (0.39 g kWh^{-1}) achieved over

Ru-Ni/$BaTiO_3$ at 25 W and 10 W, respectively. To gain insights into the physio-chemical properties of the Ru-M/$BaTiO_3$ catalysts, comprehensive catalyst characterizations were performed, including X-ray diffraction, N_2 physisorption measurements, X-ray photoelectron spectroscopy (XPS), high-resolution transmission electron microscopy (HRTEM), energy dispersive spectroscopy (EDS), and temperature-programmed desorption of CO_2 and N_2 (CO_2 and N_2-TPD). The results indicated that the loading of Ni enhanced the basicity and N_2 adsorption capacity of the catalyst surface, as well as the density of oxygen vacancy (OV) on the $BaTiO_3$ surface, which facilitated the adsorption and activation of N_2 on $BaTiO_3$ surface. These effects led to the enhanced NH_3 synthesis, as excited N_2 could be adsorbed on Ru-Ni/$BaTiO_3$ from plasma region and stepwise hydrogenated to form NH_x species and ultimately NH_3.

Keywords: plasma catalysis, ammonia synthesis, Ru-based bimetallic catalyst, oxygen vacancy, N_2 activation

1. Introduction

Besides being an essential raw material for many chemicals, ammonia (NH_3) has shown great value and environmental benefits as an emerging clean fuel due to its characteristics of carbon-free, high energy density and easy to liquid and store [1]. NH_3 can be directly used in fuel cells to generate electricity, and blended with conventional fossil fuels such as gasoline and diesel for combustion to output mechanical power [2, 3]. Using a NH_3 blend-fuel power system can achieve higher thermal efficiency and lower NO_x, SO_x, and CO_2 emissions than a fossil fuel-powered

internal combustion engine [4, 5].

Currently, the Haber-Bosch process based NH_3 synthesis is the major industrial-scale NH_3 synthesis process. This process is an energy-intensive thermal catalytic reaction that requires the reactants to be maintained within a temperature range of 450–600°C and a pressure range of 10–25 MPa for NH_3 synthesis. The Haber-Bosch process based NH_3 synthesis relies almost entirely on the combustion of fossil fuels to provide the required energy. Due to the harsh reaction conditions, the production of 1 kg of NH_3 results in emissions of 1.25–2.16 kg of CO_2 equivalent due to the harsh reaction conditions [6]. Therefore, the NH_3 synthesis industry consumes approximately 1.8–3% of global energy each year and emits approximately 290 million tons of CO_2 [7, 8].

Establishing small-scale, decentralized NH_3 production plants to utilize localized and intermittent renewable energy sources is currently the main way to produce "green ammonia". Among various technologies for the synthesis of "green ammonia", e.g. photo-catalysis [9, 10] and electro-catalysis [11, 12], the plasma-catalysis process has received widespread attention. The plasma-catalytic system could be operated under mild catalytic reaction conditions, and is easy to achieve miniaturization and decentralization of NH_3 synthesis equipment. The plasma-catalytic system is characterized by quick start and stop times, which allows it to match intermittent and seasonal renewable energy sources. This enables the conversion and storage of localized renewable energy sources. Furthermore, in the process of plasma-catalytic synthesis of NH_3, the activation of the $N{\equiv}N$ bond is mainly achieved via collisions

with energetic electrons, making NH_3 synthesis thermodynamically favorable even at ambient pressure and room temperature [13, 14].

Perovskite oxides (with the general formula ABO_3) have recently emerged as a new and promising class of catalyst support in heterogeneous catalysis due to their exceptional thermal stability, tunable electronic structure, and redox behavior [15]. Due to the unique structure of perovskite oxides, which can accommodate variable B-site elements and valences, these catalyst supports are highly susceptible to introducing interface effects, such as strong metal-support interaction (SMSI) and oxygen vacancies (OV). This, in turn, enhances the activity of ABO_3-supported catalysts for NH_3 synthesis [16, 17]. Moreover, our previous research has demonstrated that the introduction of $BaTiO_3$, with its high dielectric constant, into the plasma discharge region could amplify the electric field of the gas phase, thereby facilitating N_2 activation through electron-impact reactions, which represents the primary step in plasma-catalytic NH_3 synthesis [18].

The incorporation of metallic catalysts has been demonstrated to enhance the plasma-catalytic performance of NH_3 synthesis, as the metal sites on the catalyst support play a critical role in heterogeneous reactions [19-21]. Various metal-based catalysts have proved to be active for NH_3 synthesis to date. Among them, the Ru-based catalysts are more efficient under milder reaction conditions as they afford more prominent N_2 activation due to the proper binding strength of atomic N and N_2 dissociation barrier [22, 23]. However, the utilization of Ru-based catalysts has been limited due to the high cost and low production of Ru. To reduce cost and optimize

the performance of Ru-based metallic catalysts, alloying Ru with other metal components has been found effective in adjusting its structural and electronic properties, thereby increasing its ability to activate the N≡N bond. This approach builds upon knowledge gained from conventional thermal catalytic NH_3 synthesis. For example, previous studies have demonstrated that an alloy of Ru-Fe/MgO resulted in a higher NH_3 yield and better anti-poisoning performance compared to pure Ru and Fe catalysts [24]. Similarly, the Ru-Co/$MgAl_2O_4$ catalyst was found to be the most active among the Ru-M/$MgAl_2O_4$ catalysts (M = Fe, Co, Ni, and Mo). When the Ru loading was reduced from 4 wt.% to 2 wt.%, and Co was added at the same 2 wt.% loading in the Ru-Co/$MgAl_2O_4$ catalyst, its activity was comparable to that of the 4 wt.% Ru/$MgAl_2O_4$ catalyst, suggesting the underlying synergistic effect between bimetallic components [25]. Some studies suggested that the improved performance of Ru-based bimetallic catalysts may be attributed to different surface activities resulting from electron transfer between the metals, as well as favorable kinetics and thermodynamics of N_2 dissociation [24, 26]. Despite these efforts to investigate the mechanisms underlying for thermal-catalytic NH_3 synthesis, the understanding of the reaction mechanisms of plasma-catalytic NH_3 synthesis over Ru-based bimetallic catalysts remains limited.

In this study, we investigate the performance of plasma-catalytic NH_3 synthesis over bimetallic Ru-M/$BaTiO_3$ (M = Fe, Co, and Ni) catalysts in a dielectric barrier discharge (DBD) reactor. To gain insight into the changes in the physicochemical properties of the catalysts after incorporating M, we extensively characterized

113 Ru-M/$BaTiO_3$ catalysts using various techniques such as X-ray diffraction (XRD), N_2
114 physisorption measurements, X-ray photoelectron spectroscopy (XPS),
115 high-resolution transmission electron microscopy (HRTEM), energy dispersive
116 spectroscopy (EDS), and temperature programmed desorption (CO_2-TPD and
117 N_2-TPD). In addition, we used optical emission spectroscopy (OES) to identify the
118 reactive species during the plasma-catalytic reactions. Based on the results obtained,
119 we propose the mechanisms underlying the enhanced performance of Ru-Ni/$BaTiO_3$
120 catalysts in plasma-catalytic NH_3 synthesis.

121 **2. Experimental**

122 **2.1 Catalysts preparation and characterization**

123 Bimetallic catalysts of Ru-M/$BaTiO_3$ (M = Fe, Co and Ni) were prepared using
124 the co-impregnation method. Initially, the nitrates of M and $RuCl_3 \cdot 3H_2O$ were
125 dissolved in deionized water, then the solution was added to a measured amount of
126 $BaTiO_3$ powder. The slurry was stirred for 30 min, then heated at 80°C for 3 h, dried
127 at 110°C for 12 h, and calcined at 550°C for 6 h. The catalysts were reduced in a 5
128 vol.% H_2/Ar flow at 550°C and 100 ml min^{-1} for 3 h, then screened to 40-60 mesh.
129 The total loading amount of active metal for each catalyst was fixed at 3 wt.%, while
130 the molar ratio of Ru to M was 1:1. The catalysts were named Ru-Fe/$BaTiO_3$,
131 Ru-Co/$BaTiO_3$, Ru-Ni/$BaTiO_3$ and Ru/$BaTiO_3$. The chemicals $Ni(NO_3)_2 \cdot 6H_2O$,
132 $Co(NO_3)_2 \cdot 6H_2O$, $Fe(NO_3)_3 \cdot 9H_2O$, $RuCl_3 \cdot 3H_2O$ and $BaTiO_3$ were all of analytical
133 grade (Macklin, China). The purity of all gases (H_2, N_2, and Ar) was 99.999%
134 (Fangxin, China).

The XRD patterns of the Ru-M/$BaTiO_3$ catalysts were obtained using a Rikagu D/max-2000 X-ray diffractometer equipped with Cu-Kα radiation. The scanning range was 10° to 80°, and the scanning step size was 0.02°. N_2 physisorption measurements were performed using a Quantachrome Autosorb-1 instrument at 77 K. Before each test, the catalysts were degassed at 250 °C for 3 h to remove impurities. The specific surface area was obtained using the Brunauer-Emmett-Teller (BET) method, and pore volume and diameter distribution were obtained using Barrett Joyner Halenda (BJH) method. High-resolution transmission electron microscopy (HRTEM) and energy-dispersive X-ray spectrometry (EDS) mapping analyses were performed using the FEI Tecnai G2 F20. The particle size distribution of each catalyst was obtained by analyzing 100 particles from the TEM images.

Temperature programmed desorption (TPD) experiments were conducted on an AutoChem II 2920 instrument to measure the desorption behavior of CO_2 and N_2. Prior to the test, catalysts were reduced in a H_2/He gas flow (10 vol.% H_2; 50 mL min^{-1}) at 550°C for 2 h and then cooled to 50°C. For CO_2-TPD, the catalysts were treated in a CO_2 gas flow at 50°C and 50 ml min^{-1} for 30 min to adsorb CO_2, while for N_2-TPD, the catalysts were placed in a N_2 gas flow at 500°C and 50 ml min^{-1} for 1 h, then they were cooled to 50°C and kept for 30 min to adsorb N_2. The samples were then heated to 900°C at the rate of 10 °C min^{-1} in a He flow at the flow rate of 40 ml min^{-1} for both CO_2-TPD and N_2-TPD.

X-ray photoelectron spectroscopy (XPS) analysis was performed on a Thermo ESCALAB 250Xi using an Al Kα X-ray source. Both low-resolution survey and

high-resolution scans were obtained for each catalyst, and the spectra were calibrated with C 1s at a binding energy of 284.8 eV. Prior to the XPS analysis, the catalysts were reduced in H_2/He gas flow (10 vol.% H_2; 50 ml min^{-1}) at 550°C for 2 h and then cooled to ambient temperature. After reduction, the samples were prepared and analyzed in a reduced environment.

2.2 Experimental setup

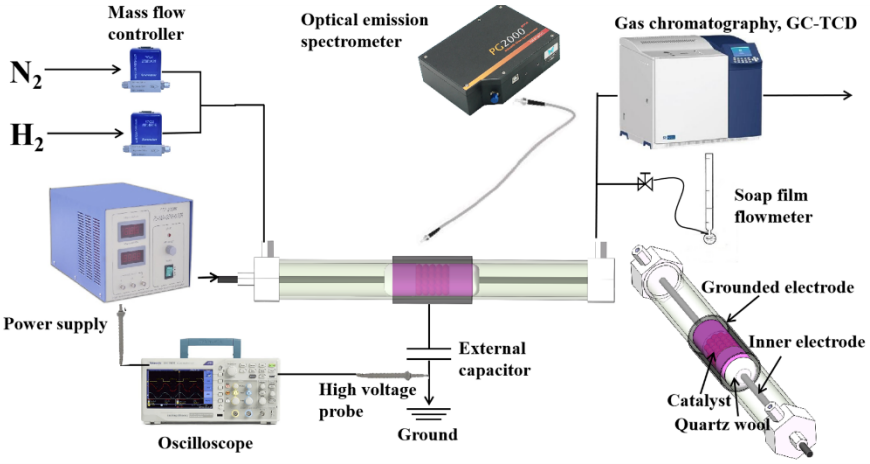

Fig. 1. Experimental setup for plasma-catalytic NH_3 synthesis

A schematic diagram of the experimental system used in this study is shown in Fig. 1. The reactor comprised a quartz tube with an inner diameter of 8 mm and a wall thickness of 2 mm, sealed with two PTFE seals. The high-voltage electrode was a 4 mm diameter stainless-steel rod connected to a power source (Suman CTP-2000K, China), while the external electrode was a stainless-steel mesh wrapped around the quartz tube. The Ru-M/$BaTiO_3$ catalyst (0.4 g, 40–60 meshes) was held in the reactor by quartz wool. High voltage probes (Tektronix TPP0502, USA) were used to

174 measure the voltages across the external capacitor (0.47 μF) and the reactor, and a
175 four-channel digital oscilloscope (Tektronix TDS2024C, USA) was used to record all
176 electrical signals.

177 N_2 and H_2 gases with a purity exceeding 99.999% were sourced from gas
178 cylinders and regulated by mass flow controllers (Sevenstars D07-B, China). The
179 gases were mixed in a chamber before being introduced to the reactor in a 1:1 molar
180 ratio. To measure the concentrations of gas products (including N_2, H_2, and NH_3), a
181 two-channel gas chromatography (Fuli 9790II, China) equipped with a thermal
182 conductivity detector (TCD) was used. Optical emission spectra during plasma
183 discharge in the presence of the Ru-M/$BaTiO_3$ catalysts were captured using an
184 optical spectrometer (Ideaoptics PG2000EX, China).

185 **2.3 Electrical characteristic measurement and parameters calculation.**

186 The plasma discharge power was calculated by the Lissajous method as follows:

$$P_{\text{dis}}(\text{W}) = f \times C_{\text{ext}} \times A \tag{1}$$

187 where C_{ext} is external capacitance (0.47 μF), f is the frequency of AC discharge (9.4 to
188 9.8 kHz), and A is the area of the Lissajous figures (Fig. S1).

189 The energy yield of the plasma-catalytic NH_3 synthesis was calculated using the
190 following equation:

$$Energy\ yield\left(\text{g kWh}^{-1}\right) = \frac{M \times C_{\text{out}} \times Q_{\text{after}}}{P_{\text{dis}}} \tag{2}$$

191

192 where M denotes the molar mass of NH_3, C_{out} is the NH_3 concentration measured at
193 the reactor outlet and Q_{after} is the gas flow rate after the reaction measured by a
194 soap-film flowmeter.

3. Results and discussion

3.1. Catalyst characterizations

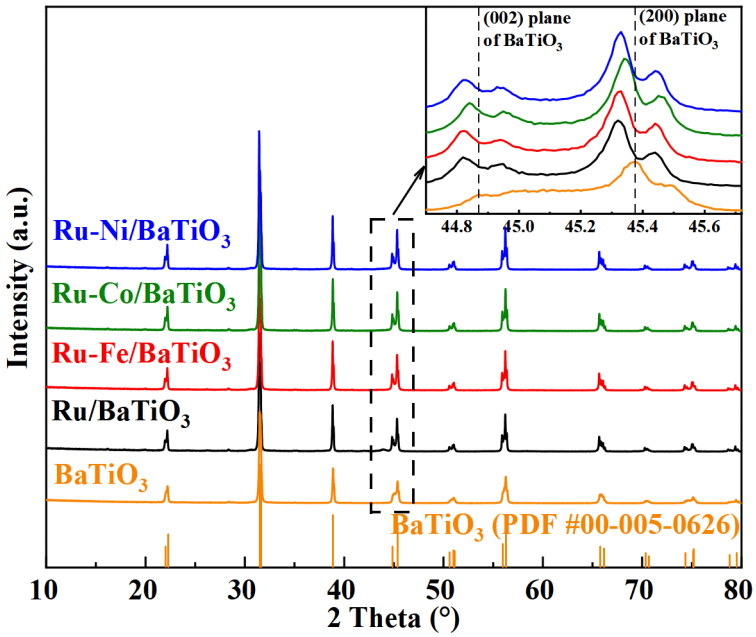

Fig. 2. XRD patterns for the Ru-M/$BaTiO_3$ catalysts

Fig. 2 depicts the XRD patterns of the Ru-M/$BaTiO_3$ catalysts used in the study. All the catalysts showed well-matched diffraction peaks with the tetragonal phase $BaTiO_3$ (ICDD PDF #00-005-0626). The diffraction peaks at 2θ of 31.49°, 31.64°, 38.88°, 44.85°, 45.37°, 55.95°, and 56.25°, which can be attributed to the (1 0 1), (1 1 0), (1 1 1), (0 0 2), (2 0 0), (1 1 2), and (2 1 1) planes of $BaTiO_3$ in the tetragonal phase, were intense for all the Ru-M/$BaTiO_3$ catalysts. No diffraction peaks of metallic Ru, Fe, Co, and Ni were observed in the XRD patterns, probably due to the high dispersion of the metal dopants on the $BaTiO_3$ support. The presence of the dopant M caused the diffraction peaks of (0 0 2) and (2 0 0) planes to shift to lower angles when compared to $BaTiO_3$, which could be associated with the lattice

expansion of $BaTiO_3$. This phenomenon might be attributed to the substitution of Ti^{4+} in $BaTiO_3$ by M cation with a larger radius(which is c.a. 0.61, 0.65, 0.61, 0.69 and 0.68 Å for Ti^{4+}, Fe^{3+}, Co^{2+}, Ni^{2+} and Ru^{3+}, respectively [27-30]), and oxygen vacancy was generated for electronic compensation, as the dopant of M cation preferentially substitutes for Ti^{4+} ions in $BaTiO_3$ due to the similarity of their ionic radii in octahedral coordination [31-33].

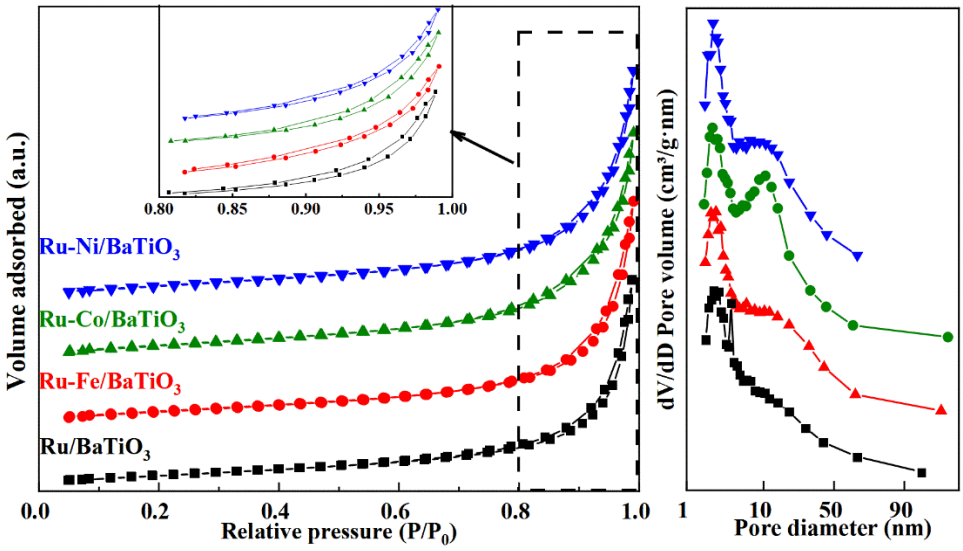

Fig. 3. N_2 adsorption-desorption isotherms and pore diameter distribution of the Ru-M/$BaTiO_3$ catalysts

As shown in Fig. 3, all Ru-M/$BaTiO_3$ samples exhibited clear characteristics of type IV isotherms with H4 hysteresis loops, indicating their mesoporous structure. Compared to Ru-M/$BaTiO_3$, the introduction of dopant M resulted in a decrease in the most probable aperture and average pore size, while the specific surface area slightly increased. For instance, the most probable aperture was 2.66 nm for Ru/$BaTiO_3$, which reduced to 2.26 nm for Ru-Ni/$BaTiO_3$ and 2.20 nm for Ru-Co/$BaTiO_3$. Meanwhile, the specific surface area increased from 2.26 $m^2\ g^{-1}$ for Ru/$BaTiO_3$ to 2.62 $m^2\ g^{-1}$ for Ru-Ni/$BaTiO_3$. Considering the structural differences among the

Ru-M/$BaTiO_3$ catalysts were not significant, it suggests that the loading of M had a limited impact on adjusting the framework structure of catalysts.

Table 1. Textural properties of the Ru-M/$BaTiO_3$ catalysts

Catalyst	S_{BET} (m^2 g^{-1})	Total pore volume (cm^3 g^{-1})	Average pore size (nm)	The most probable aperture (nm)
Ru-Fe/$BaTiO_3$	2.42	0.010	16.05	2.37
Ru-Co/$BaTiO_3$	2.57	0.011	15.05	2.20
Ru-Ni/$BaTiO_3$	2.62	0.011	15.86	2.26
Ru/$BaTiO_3$	2.26	0.010	17.18	2.66

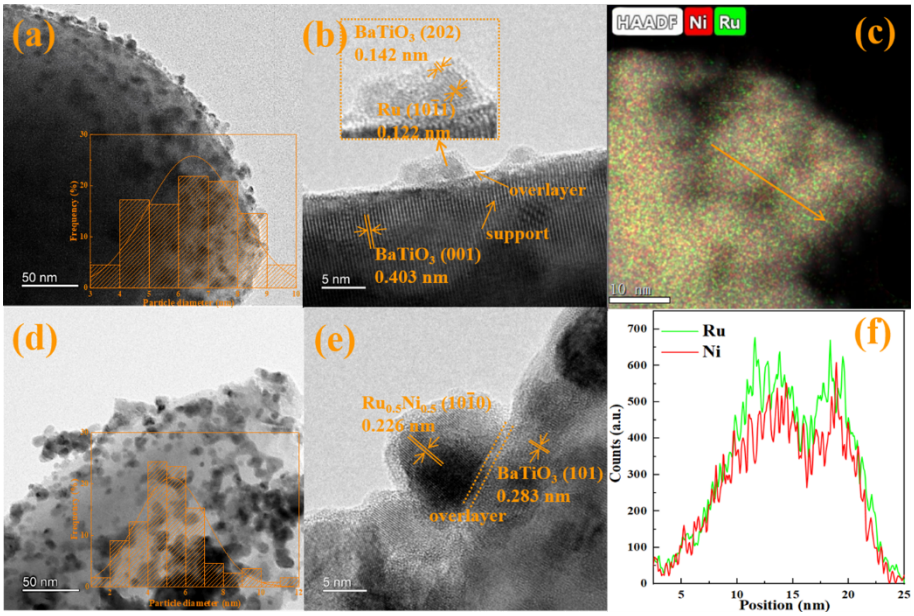

Fig. 4. HRTEM for (a and b) Ru/$BaTiO_3$, (d and e) for Ru-Ni/$BaTiO_3$; (c) EDS mapping of Ru-Ni particles on Ru-Ni/$BaTiO_3$; (f) line scanning of Ru-Ni particles

High-resolution transmission electron microscopy (HRTEM) was employed to analyze the catalysts' morphology. As depicted in Fig. 4(a) and (d), the doped metal particles were predominantly present on the support's surface in a highly disordered

state. By using EDS-mapping, the distribution of Ru and Ni elements on the surface of the $BaTiO_3$ support was investigated, and the results were shown in Fig. S2. The uniform and random distribution of Ru and Ni elements on the surface of the $BaTiO_3$ support was confirmed by comparing spatial features in both the Ru and Ni maps, which is consistent with Fig. 4(d). In comparison to Ru/$BaTiO_3$, the average size of the metal particle in Ru-Ni/$BaTiO_3$ is 3.12 nm, which is much smaller than that in Ru/$BaTiO_3$ (5.14 nm). The metal particle size of Ru-Ni/$BaTiO_3$ mainly ranged from 4–6 nm, whereas it was 6–8 nm for Ru/$BaTiO_3$. This observation is consistent with the study by Ni et al., who reported that adding Mg reduced the particle size of Ru-Mg particles and improved the dispersion of Ru nanoparticles on the surface of Ru-Mg/AC due to the interaction of metal precursors during the high-temperature reduction process [34].

Figs. 4(b) and (e) show the d-spacings of 0.206 and 0.226 nm correspond to the $(1\ 0\ \bar{1}\ 1)$ plane of Ru (ICDD PDF #00-006-0663) and $(1\ 0\ \bar{1}\ 0)$ plane of Ru-Ni alloy (ICDD PDF #04-001-2915) in the hexagonal phase, respectively. The structure of Ru-Ni binary particle was further investigated by EDS. As presented in Fig. 4(c), the location color point presenting Ru and Ni elements were uniformly mixed and covered. The line canning results showing in Fig. 4(e) suggest the intensities of Ru and Ni exhibited the same spatial trend of variation, which confirmed that Ru-Ni existed in the form of a homogeneous alloy.

Fig. 4(b) reveals that the Ru particles were doped onto and encapsulated by the $BaTiO_3$ support, which can be attributed to the SMSI effect [35]. The SMSI effect

could alter the electronic properties of active metal species by electron transfer from the support to metal particles that are doped onto the support, and further vary the adsorption strength of reactants on the metal particles [36]. However, in the case of $Ru/BaTiO_3$, the full encapsulation of the Ru particles had a detrimental effect on their catalytic activity due to the decrease in metal sites. Fig. 4(e) also confirms the occurrence of the SMSI effect in the case of $Ru\text{-}Ni/BaTiO_3$ since an overlayer is found between the Ru-Ni metal particle and the $BaTiO_3$ support.

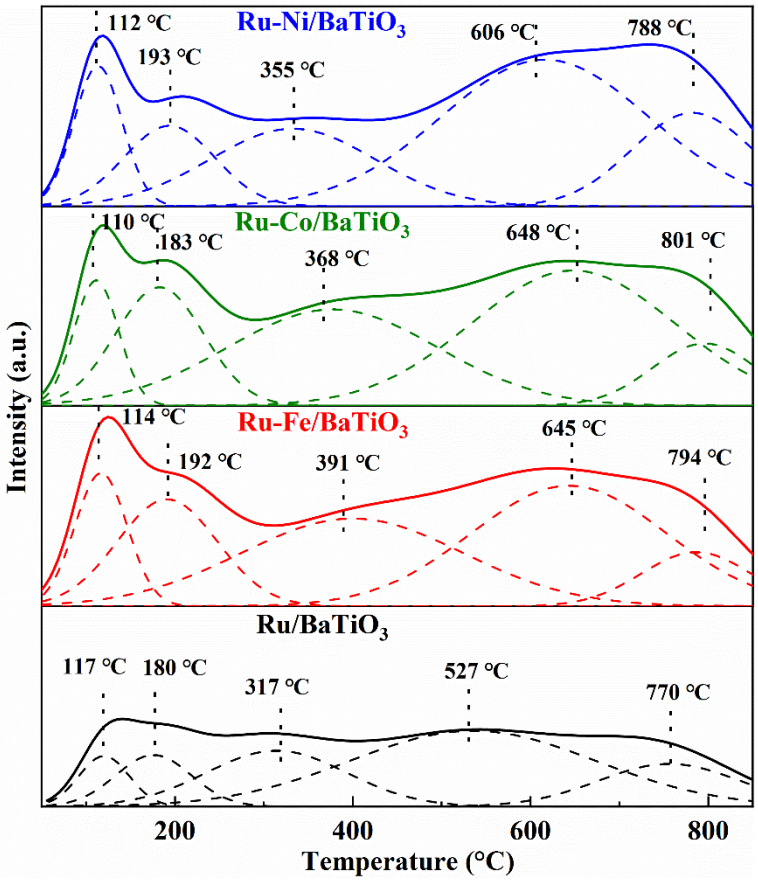

Fig. 5. CO_2-TPD profiles of the $Ru\text{-}M/BaTiO_3$ catalysts

The basicity of $Ru\text{-}M/BaTiO_3$ catalysts was evaluated using CO_2-TPD, as presented in Fig. 5. The desorption peaks centered in the low temperature region (50–

300°C) correspond to physical adsorption and the adsorption on Brønsted basicity sites of the Ru-M/$BaTiO_3$ catalysts. Meanwhile, the desorption peaks centered in the medium temperature (300–600°C) and high temperature (> 600°C) regions correspond to the desorption of CO_2 on medium and strong basic sites, respectively, indicating the desorption of CO_2 from Lewis basicity sites [37, 38]. Compared to Ru/$BaTiO_3$, the introduction of dopant M into the Ru-M/$BaTiO_3$ catalysts improved the density of both weak and strong basic sites. The increase in the density of weak basic sites in the presence of dopant M is believed to be related to the surface-adsorbed hydroxyl groups[38], while the medium and strong basicity are associated with the chemisorption on oxygen species such as electron-rich O^{2-}, O_2^{2-} and O^- species [39], which are related to CO_2 adsorption on surface OV sites [40]. To better quantify the strength of basicity in the Ru-M/$BaTiO_3$ catalysts, the CO_2-TPD profiles were deconvoluted and the amount of CO_2 desorbed was listed in Table S1. The results showed that the amount of CO_2 desorbed from medium and strong basic sites of the Ru-M/$BaTiO_3$ catalysts were 54.2 μmol g^{-1} for Ru-Ni/$BaTiO_3$, 50.5 μmol g^{-1} for Ru-Co/$BaTiO_3$, 48.2 μmol g^{-1} for Ru-Fe/$BaTiO_3$ and 31.9 μmol g^{-1} for Ru/$BaTiO_3$, respectively. These findings indicate that there was an increased density of Lewis basic sites on the surface of the Ru-M/$BaTiO_3$ catalysts, with Ru-Ni/$BaTiO_3$ exhibiting the highest density of Lewis basic sites.

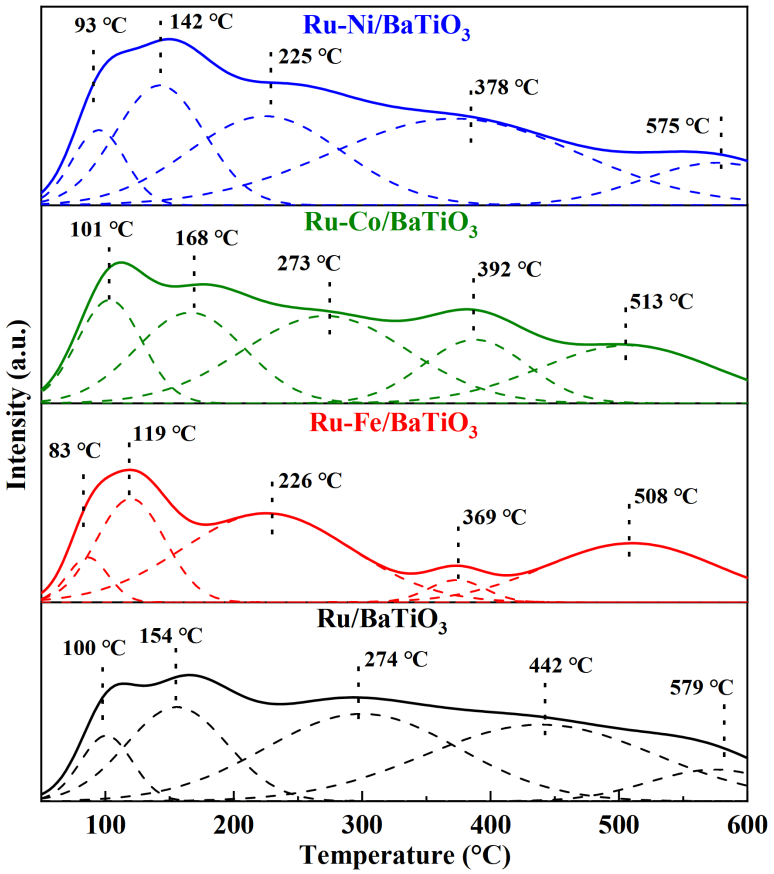

Fig. 6. N_2-TPD profiles for the Ru-M/$BaTiO_3$ catalysts

As presented in Fig. 6, the N_2-TPD desorption profiles for the Ru-M/$BaTiO_3$ catalysts can be deconvoluted into 5 peaks. The first two peaks, centered below 200°C, correspond to the desorption of physically adsorbed N_2, while the peaks centered above 200°C can be attributed to the desorption of chemisorbed N_2 [41]. In comparison to Ru/$BaTiO_3$, the desorption profile of Ru-Ni/$BaTiO_3$ catalyst showed a similar pattern with a significantly higher N_2 desorption amount. However, the introduction of Fe or Co to the catalyst resulted in the inhibition of both physical and chemical adsorption of N_2. The amount of N_2 chemisorption, which was determined by N_2 desorption amount above 200°C, follows the order of Ru-Ni/$BaTiO_3$ (53.2 μmol g^{-1}) > Ru/$BaTiO_3$ (48.8 μmol g^{-1}) > Ru-Co/$BaTiO_3$ (37.9 μmol g^{-1}) > Ru-Fe/$BaTiO_3$ (24.1 μmol g^{-1}). Such chemisorption of N_2 is necessary for N_2

activation, but the diffusion of some key intermediates, such as N and NH_x radicals that bind too strongly to the metal surface, may be impeded [42].

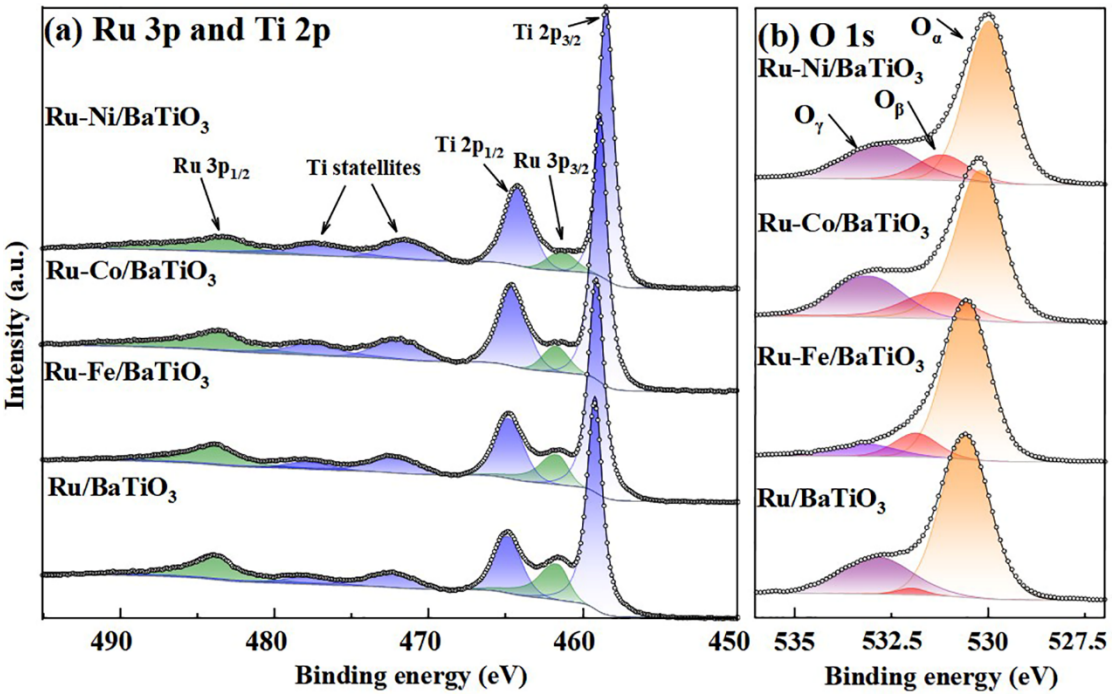

Fig. 7. High-resolution XPS spectra for Ru-M/$BaTiO_3$ catalysts: (a) Ru 3p and Ti 2p; (b) O 1s

Fig. 7(a) presents high-resolution XPS spectra of the Ru 3p and Ti 2p orbits. These spectra were deconvoluted using the Lorentzian-Gaussian function. Generally, the binding energies (BE) of Ru $3p_{1/2}$ and Ru $3p_{3/2}$ were centered around 483.7 and 461.7 eV, respectively. For Ru/$BaTiO_3$, the BE of Ru $3p_{1/2}$ was 483.92 eV, which was lower than the standard BE of Ru $3p_{1/2}$ at 484.8 eV, indicating that the Ru particles on the $BaTiO_3$ surface were in an electron-rich state [43]. The BE of Ru $3p_{1/2}$ for the Ru-M/$BaTiO_3$ catalysts further decreased compared to the Ru/$BaTiO_3$ catalyst, for example, the BE of Ru $3p_{1/2}$ for Ru-Fe/$BaTiO_3$ was 483.88 eV, while it shifted to 483.33 eV for Ru-Ni/$BaTiO_3$.

Regarding the Ti 2p spectra of the Ru-M/$BaTiO_3$ catalysts, two main peaks from the Ti $2p_{3/2}$ and Ti $2p_{1/2}$ orbits at around 459 eV and 464 eV, respectively, were clearly observed along with two satellite peaks. The BE of Ti $2p_{3/2}$ for Ru/$BaTiO_3$ was 459.28 eV, and it shifted to 458.96 eV and 458.45 eV for Ru-Fe/$BaTiO_3$ and Ru-Ni/$BaTiO_3$, respectively. The shift of characteristic peaks in the Ti $2p_{3/2}$ and Ti $2p_{1/2}$ orbits can be attribute to the generation of Ti^{3+} and are related to the generation of OV [44, 45].

Fig. 7(b) presents the high-resolution XPS spectra of the O 1s orbit for the Ru-M/$BaTiO_3$ samples. The peaks centered around 530.58 eV belong to lattice oxygen species (O_α), which mainly exists in the form of Ba-O-Ti [46]. The peaks centered around 531.90 eV correspond to O_β, which is the oxygen species in the vicinity of the OV, and the peaks centered around 533.37 eV could be attributed to surface adsorbed oxygen species (O_γ) like OH^- or O_2^{2-}, CO_3^{2-} [33, 47]. The introduction of dopant M led to the left shift of the BE of O_α and an increase in the area of O_β peaks, suggesting an increased density of OV on catalyst surface [48, 49]. The relative OV density of the Ru-M/$BaTiO_3$ catalysts, defined as $O_\beta/(O_\alpha + O_\beta + O_\gamma)$, was as follows: Ru-Ni/$BaTiO_3$ (15.35%) > Ru-Fe/$BaTiO_3$ (14.18%) > Ru-Co/$BaTiO_3$ (7.90%) > Ru/$BaTiO_3$ (1.73%). This order is in agreement with the order of the binding energy of Ti 2p.

3.2. Optical emission spectrum diagnosis

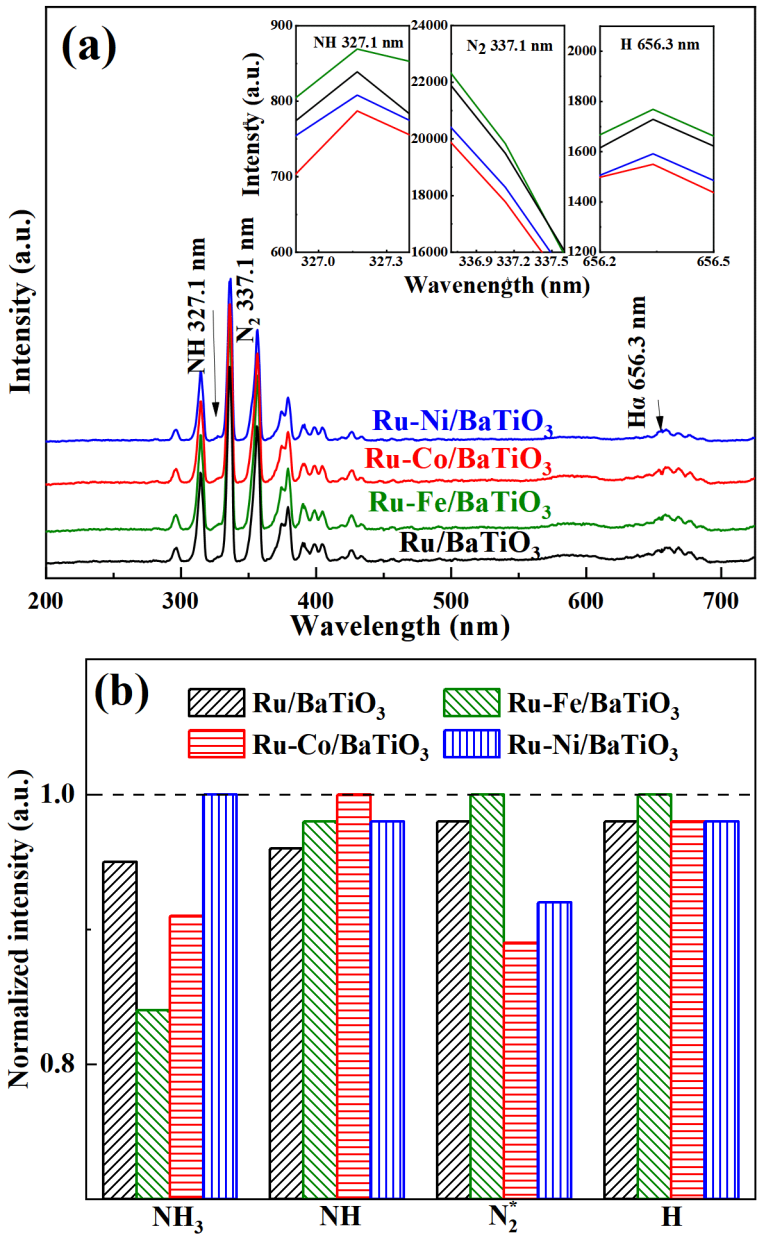

Fig. 8. (a) Optical emission spectra for plasma discharge over Ru-M/$BaTiO_3$ (plasma discharge power is 15 W and exposure time is 400 ms); (b) normalized relative intensity of reactive species

Fig. 8(a) shows the N_2 second positive system (SPS) indicating the vibrational excitation reaction of N_2. The H_α atomic line at 656.3 nm indicates the dissociation of H_2. The strong intensity of N_2 at 337 nm caused the NH band at 336.1 nm to overlap and become indistinguishable. Therefore, the NH band at 327.1 nm was chosen to determine the relative intensity of the NH bands. The selection of emission lines and

corresponding transitions are listed in Table S2. The intensities of the selected emission lines of these reactive species were normalized using the method proposed by Wang et al. [19], and the results are presented in Fig. 8(b).

As shown in Fig. 8(b), compared with $Ru/BaTiO_3$ and $Ru\text{-}Fe/BaTiO_3$, the relative intensity of N_2^* emission line was lower in the presence of $Ru\text{-}Ni/BaTiO_3$ and $Ru\text{-}Co/BaTiO_3$. Considering that the generation of N_2^* is mainly derived from electron-impact reactions in gas phase, which are a function of electron energy and electric field strength. The lower relative intensity of N_2^* suggests a lower degree of vibrational-excitation of N_2, indicating that the electric field was relatively lower for the case of $Ru\text{-}Ni/BaTiO_3$ and $Ru\text{-}Co/BaTiO_3$. For all $Ru\text{-}M/BaTiO_3$ catalysts, the relative intensity of the H atomic line was roughly the same around 0.99. In addition, $Ru\text{-}Co/BaTiO_3$ showed the highest relative intensity of the NH emission line, while $Ru\text{-}Fe/BaTiO_3$ and $Ru\text{-}Ni/BaTiO_3$ exhibit a lower relative intensity of 0.8, indicating a relatively lower concentration of NH radical generated in the plasma discharge region.

3.3. Plasma-catalytic NH_3 synthesis over $Ru\text{-}M/BaTiO_3$

3.3.1 Electrical characteristics of plasma discharge

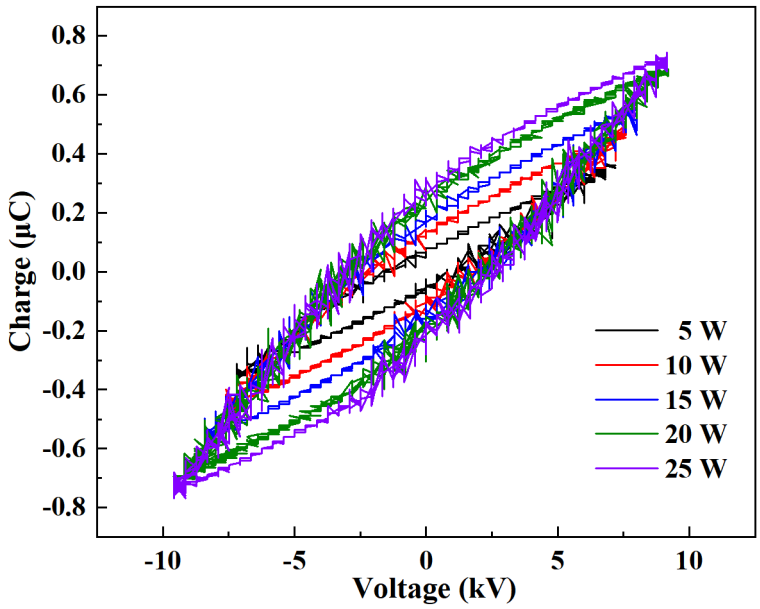

Fig. 9. Lissajous figures of Ru-Ni/$BaTiO_3$ packed DBD reactor

Fig. 9 shows that the Lissajous figures have a parallelogram shape, indicating the presence of filamentary discharge in the plasma region [50]. The Lissajous figures were used to calculate several parameters, including total capacitance (C_{cell}), effective capacitance (C_{eff}), transferred charges (Q_{trans}), and breakdown voltage (U_b), using the method described in the supporting information (Section 1). As presented in table S3, increasing the plasma discharge power resulted in a significant increase in C_{eff}, Q_{trans}, and U_b. For example, when the plasma discharge power increased from 5 W to 20 W, C_{eff} increased from 61.43 pF to 103.75 pF. The increase in C_{eff} suggests that increasing the discharge power promotes the generation of filamentary discharge channels and the spatial expansion of the plasma discharge region [51]. When the dielectric barrier is broken down, gas molecules are ionized and a large number of charged particles are generated, and electrons are directionally moved under the action of the electric field to form filamentary discharge channels [52]. As the plasma discharge power gradually increased from 5 W to 25 W, the U_b increased from 0.27

kV to 1.23 kV. The increased U_b resulted in a higher electric field strength in the plasma discharge region, and the electron escape velocity was accelerated, which promoted the development of the electron avalanche. As a result, the density of the filamentary discharge channel increased significantly, and the value of C_{eff} increased with the increase of discharge power. Considering the higher U_b and C_{eff}, it could be deduced that the discharge mode changed from partial discharge to uniform filamentary discharge when plasma discharge power increased from 5 W to 25 W. Correspondingly, the increased plasma discharge also promoted electron transfer per half-cycle via plasma discharge, which increased from 0.27 μC (5 W) to 0.97 μC (20 W).

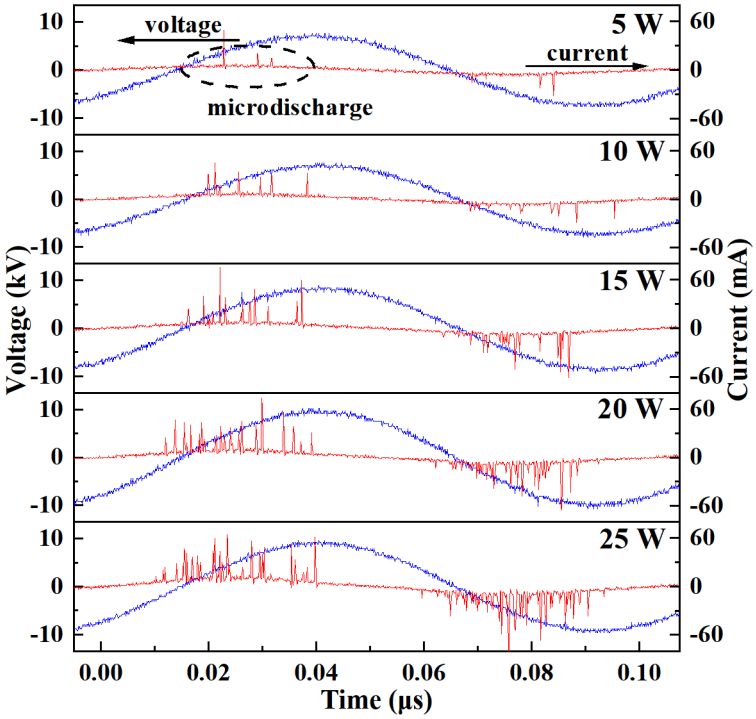

Fig. 10. *U-I* profiles of Ru-Ni/$BaTiO_3$ packed DBD reactor during plasma discharge

Fig. 10 presents the electrical signals at different plasma discharge power. Both

voltage and current waveforms exhibit a sinusoidal pattern, but with numerous spikes near the voltage peak, which further confirms the presence of filamentary discharges. The intensity and density of micro-discharges were evaluated by the spikes per discharge cycle [53]. Only a few spikes could be observed at a plasma discharge power of 5 W. Increasing the plasma discharge power enhanced the intensity and density of filamentary discharge, leading to more transferred charges and a higher effective capacitance, as confirmed by the Lissajous figures. This phenomenon confirms that increasing plasma discharge power can promote NH_3 synthesis by expanding the discharge region and increasing the number of filamentary channels. Furthermore, the Lissajous figures overlapped with each other in the presence of different Ru-M/$BaTiO_3$ catalysts as shown in Fig. S3, indicating that the dopant M has only a limited effect on plasma discharge characteristics.

3.3.2 Plasma-catalytic NH_3 synthesis performance

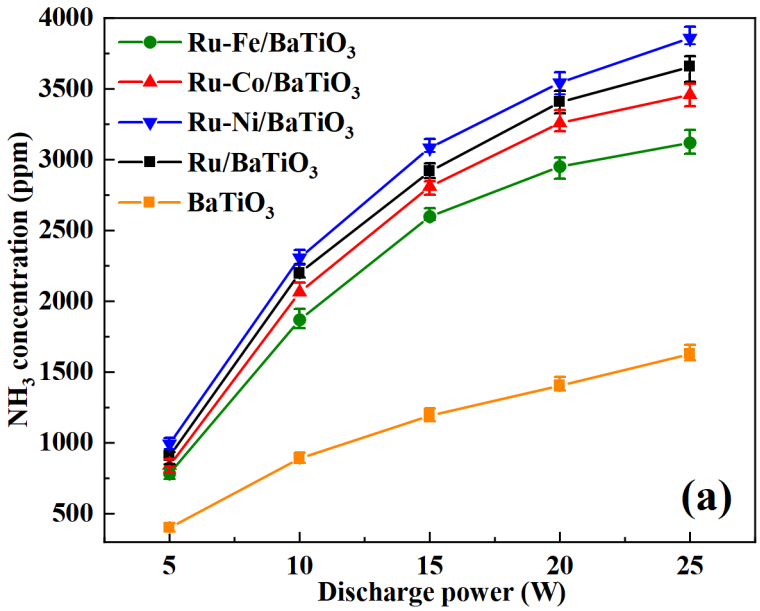

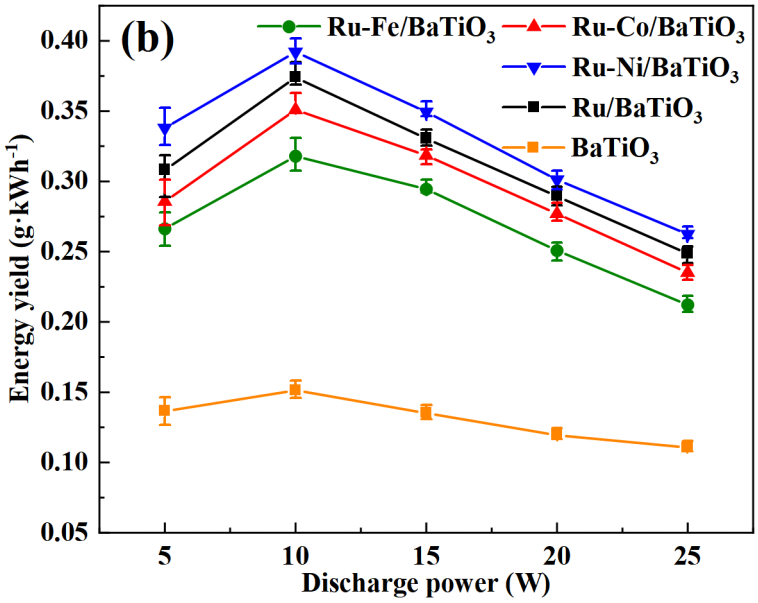

Fig. 11. Plasma-catalytic NH_3 synthesis performance over Ru-M/$BaTiO_3$ catalysts (a) outlet NH_3 concentration; (b) energy yield

Fig. 11 illustrates the NH_3 synthesis performance of Ru-M/$BaTiO_3$ (M = Fe, Co and Ni) catalysts based on the outlet NH_3 concentration at the plasma discharge power from 5 W to 25 W. It is evident that the NH_3 concentration showed an upward trend following the increasing plasma discharge power. Among the tested catalysts, Ru-Ni/$BaTiO_3$ exhibited the highest NH_3 concentration, followed by Ru/$BaTiO_3$, Ru-Co/$BaTiO_3$, Ru-Fe/$BaTiO_3$ and $BaTiO_3$ over the discharge power range. The NH_3 concentration over Ru-Ni/$BaTiO_3$ increased significantly from 994 ppm at 5 W to 3083 ppm at 15 W, and then gradually to 3895 ppm at 25 W. In contrast, the introduction of dopant Co and Fe reduced the NH_3 concentration compared to Ru/$BaTiO_3$. For all tested catalysts, the energy yield initially increased from 5 W to 10 W and then decreased from 10 W to 25 W, as shown in Fig. 11(b). Specifically, for Ru-Ni/$BaTiO_3$, the energy yield increased from 0.34 g kWh^{-1} at 5 W to 0.39 g kWh^{-1} at 10 W and then decreased to 0.26 g kWh^{-1} at 25 W. Similar trends were observed in

previous works [54, 55].

3.3.3 Enhancement mechanism of Ru-Ni/$BaTiO_3$

Instead of N_2 directly dissociating in the gas phase through electron-impact, the plasma promotes N_2 dissociation on the catalyst surface by activating N_2 to the vibrational state, which improves the dissociative sticking probability and reduces the dissociation energy barrier of N_2 on the catalyst surface, as reported in previous studies [56, 57]. In this work, we found that the relative concentration of N_2^* in the presence of Ru-Ni/$BaTiO_3$ was lower than that of Ru/$BaTiO_3$. This is likely due to the high dispersity of the Ru-Ni particles, which facilitates the breakover of plasma discharge current, but is unfavorable for enhancing the electric field [58, 59]. Based on the relatively lower degree of N_2 excitation in the presence of Ru-Ni/$BaTiO_3$, it can be deduced that the enhancement of NH_3 synthesis performance mainly results from the activation of N_2 on the catalyst surface, followed by hydrogenation through heterogeneous reactions.

The introduction of dopant M caused changes to the lattice structure of $BaTiO_3$ by partially substituting Ti^{4+}. This led to a distortion of the coordination environment of the B site in $BaTiO_3$, which facilitated the generation of OV on the support of Ru-M/$BaTiO_3$. In the present study, the density of OV was significantly increased in the presence of dopant M, with the order being Ru-Ni/$BaTiO_3$ (15.35%) > Ru-Fe/$BaTiO_3$ (14.18%) > Ru-Co/$BaTiO_3$ (7.90%) > Ru/$BaTiO_3$ (1.73%). The generation of OV on the catalyst surface enhanced the Lewis basicity of the catalysts,

459 which in turn promoted the adjacent active metal into the electron-rich state via the
460 classical SMSI effect [60]. Based on the CO_2-TPD results, the Ru-Ni/$BaTiO_3$ catalyst
461 had the highest Lewis basic sites of 54.2 μmol g^{-1}, which was 1.70 times higher than
462 that of Ru/$BaTiO_3$. Correspondingly, the BE of Ru $3p_{1/2}$ for the Ru-M/$BaTiO_3$
463 catalysts decreased further compared to the Ru/$BaTiO_3$ catalyst, indicating the higher
464 density of electron on Ru surface for the case of Ru-Ni/$BaTiO_3$. Although the
465 generation of OV may not be the only reason for the electron-rich state of Ru sites
466 considering the electron transfer from Ni to Ru, it had a positive effect on improving
467 the electron density of Ru.

468 OV has been demonstrated to act as electron traps that can effectively activate N_2
469 by depleting electrons from the vacancy and accumulating electrons on the adsorbed
470 N_2 [61, 62]. Zhang et al. have also found that higher OV densities on TiO_2 surfaces
471 led to stronger N_2 adsorption and activation capacities, suggesting that chemisorption
472 of N_2 on OV sites [63]. These findings are consistent with the observed enhancement
473 in N_2 chemisorption and increase in OV density on Ru-Ni/$BaTiO_3$ catalysts.
474 Conventionally, electron transfer occurs in M-N_2 complexes, where transitional metals
475 such as Fe, Mo, Ru, and Co donate their available d-orbital electrons to the π*
476 anti-bonding orbital to activate chemisorbed N_2. Therefore, two types of active sites
477 existed on Ru-Ni/$BaTiO_3$ and played a role in activating N_2 on the catalyst surface:
478 electron-rich metal sites and OV. The electrons in the metastable state on these active
479 sites can transfer into the anti-bonding orbital of chemisorbed N_2, promoting N_2
480 activation [63, 64]. Consequently, N_2 is converted to NH_x intermediates and

ultimately to NH_3 by stepwise hydrogenation [19, 65].

During the plasma-catalytic synthesis of NH_3 from N_2 and H_2, H radicals can also be generated through electron-impact dissociation of H_2 in the gas phase. These H species have a high probability to be adsorbed on the catalyst surface, especially on the active metal sites, resulting in hydrogen poisoning of catalyst [19, 66]. This indicates that abundant H atoms cover the active sites of Ru catalysts, inhibiting the dissociative adsorption of N_2 on the metal surface and thereby limiting NH_3 synthesis [67]. In addition to promoting the activation and dissociation of adsorbed N_2, OV can also accept H atoms from the Ru surface, leading to the formation of H atoms confined in OV (OV_{-H}). This process helps to suppress hydrogen poisoning and promotes the regeneration of active metal sites [68]. The HRTEM images confirmed that the SMSI effect was successfully induced in $Ru/BaTiO_3$ and $Ru\text{-}Ni/BaTiO_3$, which can inhibit hydrogen adsorption on the active metal sites and, consequently, facilitate N_2 dissociation on catalyst surfaces [38]. However, it was observed that the metal particles tend to be fully encapsulated in $Ru/BaTiO_3$, indicating a strong SMSI effect that could decrease the number of active metal sites as larger metal particles are more likely to be encapsulated by the migrated support, which could further limit the accessibility of active sites [69]. By doping with Ni, the overlayer generated by the SMSI effect only occurs at the interfaces between the Ru-Ni alloy and $BaTiO_3$ support probably due to its smaller size distribution of the metal particles [35]. This way, the SMSI effect can maintain the electron transfer capacity with few active sites being covered.

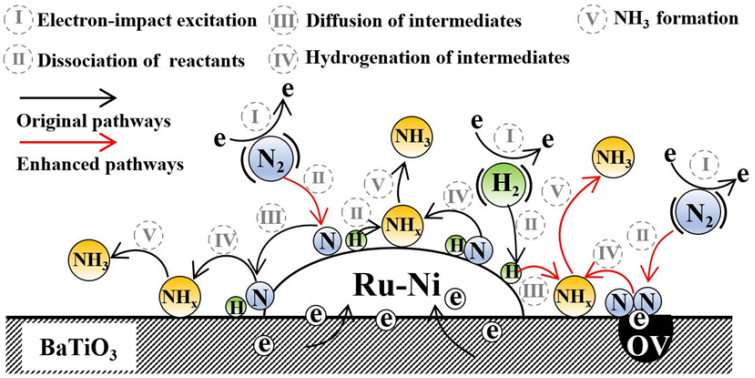

Fig. 12. Proposed mechanisms of plasma-catalytic NH_3 synthesis over Ru-Ni/$BaTiO_3$ catalyst

Based on the preceding discussions, Fig. 12 summarizes the possible enhancement mechanisms for NH_3 synthesis by plasma-catalysis over Ru-Ni/$BaTiO_3$. The superior NH_3 synthesis performance of Ru-Ni/$BaTiO_3$ over Ru/$BaTiO_3$ was mainly attributed to the enhanced surface reactions. The key enhanced reactions are described below: The NH_3 synthesis process over Ru-Ni/$BaTiO_3$ commenced with the electron-impact excitation of reactants (R1). In particular, these reactions pre-activated N_2 and facilitated its chemisorption on the catalyst surface for further activation and dissociation (R2). The introduction of Ni promoted Ru-Ni to be in an electron-rich state, which facilitated the dissociation of reactants on the metal surface and generated surface-adsorbed N and H species (R3). These N and H species could diffuse from metal sites to the support (R4). The introduction of Ni also resulted in an increased density of OV, which was a newly-generated active site for N_2 activation (R5). Consequently, Ru-Ni/$BaTiO_3$ significantly promoted N_2 surface-dissociation reactions, leading to an improvement in the concentration of N reactive species on the catalyst surface. These adsorbed N reactive species could react with abundant H radicals in the gas-phase (via E-R mechanism, R6) and on the surface (via L-H

523 mechanism, R7). As a result, more NH_x (x = 1 or 2) species could be generated
524 through the stepwise hydrogenation of N radicals, and NH_3 generation was
525 accelerated finally (R8).

$$N_2 \text{ or } H_2 + e^* \rightarrow N_2^* \text{ or } H_2^* + e \quad \text{(R1)}$$

$$N_2^* \rightarrow N_2^*(s), \text{ on catalyst surface} \quad \text{(R2)}$$

$$N_2^*(s) \text{ or } H_2^*(s) \rightarrow N\cdot(s) \text{ or } H\cdot(s), \text{ on metal sites} \quad \text{(R3)}$$

$$N\cdot(s) \text{ or } H\cdot(s), \text{ on metal sites} \rightarrow N\cdot(s) \text{ or } H\cdot(s), \text{ on support} \quad \text{(R4)}$$

$$N_2(s) + OV \rightarrow N_2^*(s) + OV \rightarrow 2N\cdot(s) + OV \quad \text{(R5)}$$

$$N\cdot(s) + xH\cdot(g) \rightarrow NH_x(s) \quad \text{(R6)}$$

$$N\cdot(s) + xH\cdot(s) \rightarrow NH_x(s) \quad \text{(R7)}$$

$$NH_x(s) + (3\text{-}x)H(s) \rightarrow NH_3(s) \rightarrow NH_3(g) \quad \text{(R8)}$$

526

527 **4. Conclusion**

528 Plasma-catalytic NH_3 synthesis was carried out using Ru-based bimetallic
529 catalysts (Ru-M/$BaTiO_3$, M = Fe, Co and Ni). The NH_3 synthesis performance was
530 observed to follow the order of Ru-Ni/$BaTiO_3$ > Ru/$BaTiO_3$ > Ru-Co/$BaTiO_3$ >
531 Ru-Fe/$BaTiO_3$, with the highest NH_3 concentration (3895 ppm) and energy yield (0.39
532 g kWh^{-1}) obtained over Ru-Ni/$BaTiO_3$ at 25 W and 10 W, respectively.

533 The effect of dopant M in the Ru-M/$BaTiO_3$ catalysts and its effect on
534 plasma-catalytic NH_3 synthesis were investigated. The basicity of the catalyst was
535 found to increase after being loaded with M, while the loading of Ni strengthened the
536 N_2 adsorption capacity of the catalyst. Compared to Ru/$BaTiO_3$, the introduction of

dopant Ni increases the density of Lewis basic sites and amount of chemisorbed N_2 on the surface of Ru-Ni/$BaTiO_3$, which were 1.70 times and 1.09 times higher, respectively. The Ru-Ni/$BaTiO_3$ catalyst also had a smaller metal particle size, which prevented the encapsulation of Ru-Ni particles by the $BaTiO_3$ support, improving the accessibility of active metal sites for NH_3 synthesis compared to Ru/$BaTiO_3$. On the one hand, these properties increased the amount of chemisorbed N_2 on the catalyst surface. On the other hand, they increased the electron density on the surface of Ru. These facilitate the activation of N_2 on the metal sites via the electron-donating effect, as well as on the catalyst surface. As a result, N_2 could be stepwise hydrogenated to form NH_x species and ultimately NH_3. This study demonstrated that the incorporation of dopant Ni could be an effective means of further improving catalyst activity in the plasma-catalytic NH_3 synthesis process, as it could act as both an electronic and structural promoter in Ru-based bimetallic catalysts.

Acknowledgment

This work was supported by the National Natural Science Foundation of China (No. 51976093).

References

1. R.H. Dolan, J.E. Anderson, T.J. Wallington, Outlook for ammonia as a sustainable transportation fuel. Sustainable Energy Fuels, 5(2021): 4830-4841.
2. D. Erdemir, Dincer I., A perspective on the use of ammonia as a clean fuel: Challenges and solutions. Int. J. Energy Res., 4 (2021): 4827-4834.
3. D. Zhou, R. Zhou, R. Zhou, B. Liu, T. Zhang, Y. Xian, P.J. Cullen, X. Lu, K. Ostrikov, Sustainable ammonia production by non-thermal plasmas: Status, mechanisms, and opportunities. Chem. Eng. J., 421(2021): 129544.
4. A. Yousefi, H. Guo, S. Dev, B. Liko, S. Lafrance, Effects of ammonia energy fraction and diesel injection timing on combustion and emissions of an ammonia/diesel dual-fuel engine. Fuel, 314(2022): 122723.

5. Lasocki, J., M. Bednarski, M. Sikora, Simulation of ammonia combustion in dual-fuel compression-ignition engine. IOP Conf. Ser. Earth Environ. Sci., 214(2019): 012081.
6. A.G. Olabi, M.A. Abdelkareem, M.A. Murisi, N. Shehata, A.H. Alami, A. Radwan, T. Wilberforce, K. Chae, E.T. Sayed, Recent progress in Green Ammonia: Production, applications, assessment; barriers, and its role in achieving the sustainable development goals. Energy Convers. Manage., 277(2023): 116594.
7. Z. Wan, Y. Tao, J. Shao, Y. Zhang, H. You, Ammonia as an effective hydrogen carrier and a clean fuel for solid oxide fuel cells. Energy Convers. Manage., 228(2021): 113729.
8. F. Gorky, J.M. Lucero, J.M. Crawford, B.A. Blake, S.R. Guthrie, M.A. Carreon, M.L. Carreon, Insights on cold plasma ammonia synthesis and decomposition using alkaline earth metal-based perovskites. Catal. Sci. Technol., 11(2021): 5109-5118.
9. Y. Huang, N. Zhang, Z. Wu, X. Xie, Artificial nitrogen fixation over bismuth-based photocatalysts: fundamentals and future perspectives. J. Mater. Chem. A, 8(2020): 4978-4995.
10. M.H. Vu, M. Sakar, T.O. Do, Insights into the recent progress and advanced materials for photocatalytic nitrogen fixation for ammonia (NH_3) production. Catalysts, 8(2018): 621.
11. A. Wu, J. Yang, B. Xu, X. Wu, Y. Wang, X. Lv, Y. Ma, A. Xu, J. Zheng, Q. Tan , Y. Peng, Z. Qi , H. Qi , J. Li, Y. Wang, J. Harding , X. Tu, A. Wang, J. Yan, X. Li, Direct ammonia synthesis from the air via gliding arc plasma integrated with single atom electrocatalysis. Appl. Catal., B, 299(2021): 120667.
12. A. Chen, B. Xia, Ambient dinitrogen electrocatalytic reduction for ammonia synthesis. J. Mater. Chem. A, 7(2019): 23416-23431.
13. L.R. Winter, B. Ashford, J. Hong, A.B. Murphy, J.G. Chen, Identifying surface reaction intermediates in plasma catalytic ammonia synthesis. ACS Catal., 10(2020): 14763-14774.
14. A. Vojvodic, A.J. Medford, F. Studt, F.A. Pedersen, T.S.Khan, T. Bligaard, J.K. Ngrskov, Exploring the limits: A low-pressure, low-temperature Haber-Bosch process. Chem. Phys. Lett., 598(2014): 108-112.
15. H. Zhu, P. Zhang, S. Dai, Recent Advances of lanthanum-based perovskite oxides for catalysis. ACS Catal., 5(2015): 6370-6385.
16. H. Fang, D. Liu, Y. Luo, Y. Zhou, S. Liang, X. Wang, B. Lin, L. Jiang, Challenges and opportunities of Ru-based catalysts toward the synthesis and utilization of ammonia. ACS Catal., 12(2022): 3938-3954.
17. V.S. Marakatti, E.M. Gaigneaux, Recent advances in heterogeneous catalysis for ammonia synthesis. Chemcatchem, 12(2020): 5838-5857.
18. J. Liu, X. Zhu, X. Hu, X. Tu, Plasma-assisted ammonia synthesis in a packed-bed dielectric barrier discharge reactor: roles of dielectric constant and thermal conductivity of packing materials. Plasma Sci. Technol., 24(2022): 025503.
19. Y. Wang, M. Craven, X. Yu, J. Ding, P. Bryant, J. Huang, X. Tu, Plasma-enhanced catalytic synthesis of ammonia over a Ni/Al_2O_3 catalyst at near-room temperature: Insights into the importance of the catalyst surface on the reaction mechanism. ACS Catal., 9(2019): 10780-10793.
20. L. Dou, Y. Liu, Y. Gao, J. Li, X. Hu, S. Zhang, K. Ostrikov, T. Shao, Disentangling metallic cobalt sites and oxygen vacancy effects in synergistic plasma-catalytic CO_2/CH_4

609 conversion into oxygenates. Appl. Catal. B, 318(2022): 121830.
610 21. X. Hu, X. Zhu, X. Wu, Y. Cai, X. Tu, Plasma-enhanced NH_3 synthesis over activated
611 carbon-based catalysts: Effect of active metal phase. Plasma Processes Polym., 17(2020):
612 2000072.
613 22. Y. Gong, H. Li, C. Li, X. Bao, H. Hosono, J. Wang, Insight into rare-earth-incorporated
614 catalysts: The chance for a more efficient ammonia synthesis. J. Adv. Ceram.,
615 11(2022): 1499-1529.
616 23. T. Wang, F.A. Pedersen, Achieving industrial ammonia synthesis rates at near-ambient
617 conditions through modified scaling relations on a confined dual site. Proc. Natl. Acad.
618 Sci. U. S. A., 118(2021): e2106527118.
619 24. K.K. Ghuman, K. Tozaki., M. Sadakiyo, S. Kitano, T. Oyabe, M. Yamauchi, Tailoring
620 widely used ammonia synthesis catalysts for H and N poisoning resistance. Phys. Chem.
621 Chem. Phys., 21(2019): 5117-5122.
622 25. Z. Yang, W. Guo, J. Lin, D. Liao, Supported catalysts with Ru-M (M = Fe, Co, Ni, Mo)
623 bimetallic active centers for ammonia synthesis. Chin. J. Catal., 27(2006): 378-380.
624 26. M.J. Banisalman, M.C. Kim, S.S. Han, Origin of enhanced ammonia synthesis on Ru-Co
625 catalysts unraveled by density functional theory. ACS Catal., 12(2022): 1090-1097.
626 27. L. Ju, T. Sabergharesou, K.G. Stamplecoskie, M. Hegde, T. Wang, N.A. Combe, H. Wu,
627 P.V. Radovanovic, Interplay between size, composition, and phase transition of
628 canocrystalline Cr^{3+}-doped $BaTiO_3$ as a path to multiferroism in perovskite-type oxides. J.
629 Am. Chem. Soc., 134(2012): 1136-1146.
630 28. M. Arshad, W. Khan, M. Abushad, M. Nadeem, S. Husain, A. Ansari, V.K. Chakradhary,
631 Correlation between structure, dielectric and multiferroic properties of lead free Ni
632 modified $BaTiO_3$ solid solution. Ceram. Int., 46(2020): 27336-27351.
633 29. C. Calle, J.A. Alonso, L. Martínez, M. Retuerto, H. García, M.T. Fernández, Ru-Ru
634 metal-metal bonding in the chains of edge-sharing octahedra of $NdMn_{1.5}Ru_{0.5}O_5$: A
635 neutron powder diffraction and magnetic study. Eur. J. Inorg. Chem., 5(2010): 781-789.
636 30. Y. Hamasaki, T. Shimizu, S. Yasui, T. Taniyama, M. Itoh, Evidence of ferroelectricity in
637 ferrimagnetic kappa-Al_2O_3-type $In_{0.25}Fe_{1.75}O_3$ films. Appl. Phys. Lett., 16(2016): 162901.
638 31. W. Peng, L. Li, S. Yu, P. Yang, K. Xu, Dielectric properties, microstructure and charge
639 compensation of MnO_2-doped $BaTiO_3$-based ceramics in a reducing atmosphere. Ceram.
640 Int., 47(2021): 29191-29196.
641 32. J. Wang, J. Leroy, G. Niu, G.S. Giron, B. Gautier, B. Vilquin , N. Barrett, Chemistry and
642 structure of $BaTiO_3$ ultra-thin films grown by different O_2 plasma power. Chem. Phys.
643 Lett., 592(2014): 206-210.
644 33. K. Xu, G. Zhu , H. Xu, Y. Zhao, K. Jiang, X. Zhang, H. Yin, M. Shangguan, L. Wan, T.
645 Huang, The colossal permittivity effect on $BaTiO_3$ induced by different sinter atmosphere.
646 Appl. Phys. A: Mater. Sci. Process., 128(2022): 1044.
647 34. J. Ni, R. Wang, F. Kong, T. Zhang, J. Lin, B. Lin, K. Wei, Highly efficient Ru-Ba/AC
648 catalyst promoted by magnesium for ammonia synthesis. Chin. J. Catal., 32(2011):
649 436-439.
650 35. Y. Guo, S. Mei, K. Yuan, D. Wang, H. Liu, C. Yan, Y. Zhang, Low-temperature CO_2
651 methanation over CeO_2-supported Ru single atoms, nanoclusters, and nanoparticles
652 competitively tuned by strong metal-support interactions and H-spillover effect. ACS

Catal., 8(2018): 6203-6215.
36. M.W. Arshad, Y. You, Y. Kim, L. Heo, S. Kim, Effect of the support material of IrRu catalysts on CO-assisted NO_x reduction. Chem. Eng. J., 455(2023): 140911.
37. H. Ronduda, M. Zybert, W. Patkowski, A. Tarka，P. Jodtowski , L. Kepinski , A. Sarnecki , D. Moszynski, W. R. Pilecka, Tuning the catalytic performance of Co/Mg-La system for ammonia synthesis via the active phase precursor introduction method. Appl. Catal. A, 598(2020): 117553.
38. Z. Wang, B. Liu, J. Lin, Highly effective perovskite-type $BaZrO_3$ supported Ru catalyst for ammonia synthesis. Appl. Catal. A, 458(2013): 130-136.
39. J. Hao, F. Cai, J. Wang, Y. Fu, J. Zhang, Y. Sun, The effect of oxygen vacancy of alkaline-earth metal Sr doped $Sm_2Zr_2O_7$ catalysts in the oxidative coupling of methane. Chem. Phys. Lett., 771(2021): 138562.
40. D. Yu, J. He, T. Xie, J. Yang , J. Wang , J. Xie, H. Shi, Z. Gao, B. Xiang , D.D. Dionysiou, boosting catalytic activity of $SrCoO_{2.52}$ perovskite by Mn atom implantation for advanced peroxymonosulfate activation. J. Hazard. Mater., 442(2023): 130085.
41. H. Ma, Z. Shi, Q. Li, S. Li, Preparation of graphitic carbon nitride with large specific surface area and outstanding N_2 photofixation ability via a dissolve-regrowth process. J. Phys. Chem. Solids, 99(2016): 51-58.
42. A.R. Singh, J.H. Montoya, B.A. Rohr, C. Tsai, A. Vovodic, J.K. Narskov, Computational design of active site structures with improved transition-state scaling for ammonia synthesis. ACS Catal., 8(2018): 4017-4024.
43. Y. Zhan, C. Zhou, F. Jin, C. Chen, L. Jiang, Ru/TiO_2 catalyst for selective hydrogenation of benzene: Effect of surface hydroxyl groups and spillover hydrogen. Appl. Surf. Sci., 525(2020): 146627.
44. Z. Han, C. Choi, S. Hong, T. W, Y. Soo, Y. Lung, J. Qiu, Z. Sun, Activated TiO_2 with tuned vacancy for efficient electrochemical nitrogen reduction. Appl. Catal. B, 257(2019): 117896.
45. H. Chen, S. Tosoni, G. Pacchioni, Adsorption of ruthenium atoms and clusters on anatase TiO_2 and tetragonal ZrO_2(101) surfaces: A comparative DFT study. J. Phys. Chem. C, 119(2015): 10856-10868.
46. J.L. Clabel., I.T. Awan, G. Lozano, M.A. Pereira-da-Silva, R.A. Romano, V.A.G. Rivera, S.O. Ferreira, E. Marega, Understanding the electronic properties of $BaTiO_3$ and Er^{3+} doped $BaTiO_3$ films through confocal scanning microscopy and XPS: the role of oxygen vacancies. Phys. Chem. Chem. Phys., 22(2020): 15022-15034.
47. J. Zhu, L. Song, J. Jiang, Y. Xiong, N. Zhang, X. Li, H. Ye, S. Chen, H. Ju, D. Liu, Y. Lin, W. Ye, C. Wang, Q. Xu, Oxide defect engineering enables to couple solar energy into oxygen activation. J. Am. Chem. Soc., 138(2016): 8928-8935.
48. H. Han, S. Jin, S. Park, Y. Kim, D. Jang, M.H. Seo, W.B. Kim, Plasma-induced oxygen vacancies in amorphous MnO_x boost catalytic performance for electrochemical CO_2 reduction. Nano Energy, 79(2021): 105492.
49. H. Zhou, M. Wang, F. Wang, Oxygen-vacancy-mediated catalytic methanation of lignocellulose at temperatures below 200 degrees C. Joule, 5(2021): 3031-3044.
50. F.A. Herrera, G.H. Brown, P. Barboun, N. Turan, P. Mehta, W.F. Schneider, J.C. Hicks, D.B. Go, The impact of transition metal catalysts on macroscopic dielectric barrier

discharge (DBD) characteristics in an ammonia synthesis plasma catalysis reactor. J. Phys. D: Appl. Physics, 52(2019): 224002.
51. X. Tu, H.J. Gallon, M.V. Twigg, P.A. Gorry, J.C. Whitehead, Dry reforming of methane over a Ni/Al_2O_3 catalyst in a coaxial dielectric barrier discharge reactor. J. Phys. D: Appl. Phys., 44(2011): 274007.
52. D.P. Subedi, U.M. Joshi, C.S. Wong, Dielectric barrier discharge (DBD) plasmas and their applications, Plasma Sci. Technol. for Emerging Econ (2017). Springer, Singapore.
53. B.S. Patil, A.S.R. Kaathoven, F.J.J. Peeters, N. Cherkasov, J. Lang, Q. Wang, V. Hessel, Deciphering the synergy between plasma and catalyst support for ammonia synthesis in a packed dielectric barrier discharge reactor. J. Phys. D: Appl. Phys., 53(2020): 144003.
54. P. Peng, Y. Li, Y. Cheng, S. Deng, P. Chen, R. Ruan, Atmospheric pressure ammonia synthesis using non-thermal plasma assisted catalysis. Plasma Chem. Plasma Process. 36(2016): 1201-1210.
55. X. Zhu, J. Liu, X. Hu, Z. Zhou, X. Li, W. Wang, R. WU, X. Tu. Plasma-catalytic synthesis of ammonia over Ru-based catalysts: Insights into the support effect. J. Energy Inst. 102(2022): 240-246.
56. K.H.R. Rouwenhorst, H.G.B. Burbach, D.W. Vogel, J.N. Paulí, B. Geerdink, L. Lefferts, Plasma-catalytic ammonia synthesis beyond thermal equilibrium on Ru-based catalysts in non-thermal plasma. Catal. Sci. Technol., 11(2021): 2834-2843.
57. K.H.R. Rouwenhorst, L. Lefferts, On the mechanism for the plasma-activated N_2 dissociation on Ru surfaces. J. Phys. D: Appl. Phys., 54(2021): 393002.
58. N. Naude, F. Massines, Influence of the surface conductivity on the stability of a glow dielectric-barrier discharge. IEEE Trans.Plasma Sci., 36(2008): 1322-1323.
59. R. Pribyl, P. Stastny, M. Pazderka, J. Kelar, Z.K. Tucekova, M. Zemanek, M. Trunec, M. Cernak, Properties of $MgAl_2O_4$ doped alumina barrier layers for dielectric barrier discharge. J. Phys. D: Appl. Phys., 53(2020): 505202.
60. X. Liu, M. Liu, Y. Luo, C. Mou, S.D. Lin, H. Cheng, J. Chen, J. Lee, T. Lin, Strong metal-support interactions between gold nanoparticles and ZnO nanorods in CO oxidation. J. Am. Chem. Soc., 134(2012): 10251-10258.
61. H. Li, J. Shang, Z. Ai, L. Zhang, Efficient visible light nitrogen fixation with BiOBr nanosheets of oxygen vacancies on the exposed {001} facets. J. Am. Chem. Soc., 137(2015): 6393-6399.
62. S. Wang, X. Hai, X. Ding, K. Chang, Y. Xiang, X. Meng, Z. Yang, H. Chen, J. Ye, Light-switchable oxygen vacancies in ultrafine Bi_5O_7Br nanotubes for boosting solar-driven nitrogen fixation in pure water. Adv. Mater., 29(2017): 1701774.
63. G. Zhang, X. Yang, C. He, P. Zhang, H. Mi, Constructing a tunable defect structure in TiO_2 for photocatalytic nitrogen fixation. J. Mater. Chem. A, 8(2020): 334-341.
64. X. Li, S. Ma, F. Luo, Z. Yang, Engineering oxygen vacancies in Co_3O_4 to boost p-d hybridization for hydrogeneration of nitrogen and oxygen. Appl. Surf. Sci., 600(2022): 154115.
65. P. Peng, Y. Li, Y. Cheng, S. Deng, P. Chen, R. Ruan, Atmospheric pressure ammonia synthesis using non-thermal plasma assisted catalysis. Plasma Chem. Plasma Process., 36(2016): 1201-1210.
66. J. Sun, Q. Chen, X. Zhao, H. Lin, W. Qin, Kinetic investigation of plasma catalytic

synthesis of ammonia: insights into the role of excited states and plasma-enhanced surface chemistry. Plasma Sources Sci. Technol., 31(2022): 094009.

67. J. Huang, M. Yuan, X. Li, Y. Wang, M. Li, J. Li, Z. You, Inhibited hydrogen poisoning for enhanced activity of promoters-Ru/$Sr_2Ta_2O_7$ nanowires for ammonia synthesis. J. Catal. 389(2020): 556-565.

68. J. Huang, J. Pan, Z. You, X. Jiang, Enhanced ammonia synthesis activity of Ru/$Ba_5Ta_4O_{15}$ catalyst by reduction of $Ba_5Ta_4O_{15}$ with CaH_2. Int. J. Hydro. Energy, 47(2022): 28019-28024.

69. Z. Luo, G. Zhao, H. Pan, W. Sun, Strong metal-support interaction in heterogeneous catalysts. Adv. Energy Mater., 12(2022): 2201395.